





Grain boundary stabilization in polar skyrmion lattices via quasiparticle-based mechanism

Kohta Kasai ^{*}, Shun Miyata , Susumu Minami , and Takahiro Shimada [†]

Department of Mechanical Engineering and Science, Kyoto University, Nishikyo-ku, Kyoto 615–8540, Japan



(Received 26 April 2025; revised 14 July 2025; accepted 3 September 2025; published 22 September 2025)

Polar skyrmions and skyrmion lattices (SkX) in ferroelectrics have attracted much attention due to their novel and unique physical properties as quasiparticles. By analogy with conventional lattice crystals, the understanding of lattice defects, particularly grain boundaries, is crucial for elucidation of the unique lattice properties hidden in the polar SkX. The fundamental structure of grain boundaries in polar SkX, however, still remains undeveloped. Here, we show that the grain boundaries in polar SkX not only have a unique lattice structure with giant skyrmion deformation, but also “quasiparticle-based” stabilization in which local lattice mismatch is maintained without relaxation. Our phase-field simulations reveal that skyrmion grain boundaries undergo structural changes accompanied by skyrmion deformation depending on the electric field and temperature conditions. Furthermore, a transition of the stabilization mechanisms occurs, where relaxation due to the movement of skyrmions is replaced by skyrmion deformation, and local giant lattice mismatch is maintained. Our findings provide unique insights into the physical properties and formation processes of polar skyrmion lattices.

DOI: [10.1103/xk7g-v1c7](https://doi.org/10.1103/xk7g-v1c7)

I. INTRODUCTION

Skyrmions are novel topological orders arising from the arrangement of electric polarization in ferroelectrics [1,2], spin configurations in magnetic materials [3,4], or other physical vectors in various systems [5,6]. Due to the topological protection, skyrmions exist independently and stably [7]. Despite being organized as continuous vector fields, skyrmions behave as individual particles and are treated as quasiparticles. Since the discovery of magnetic skyrmions in 2009 [3], they have attracted significant attention due to their exotic physical properties, such as the topological Hall effect [8], and their potential applications as racetrack memory [9], logic devices [10,11], image recognition elements [12], and neuromorphic computing devices [13]. While extensive pioneering research has been conducted on magnetic skyrmions, an increasing number of studies have also focused on polar skyrmions [14–16]. Notably, polar skyrmions exhibit unique properties not observed in magnetic skyrmions, including high-density configurations for memory applications [17], local negative permittivity [18], and optical response properties [19].

These distinctive features of polar skyrmions make them promising candidates for electric devices and other advanced engineering applications.

Since skyrmions generally arrange in large numbers on a two-dimensional plane to form a lattice [4,20,21], not only on individual skyrmions but also on the collective properties of skyrmion lattices have been focused on. Similar to conventional atomic crystals, skyrmion lattices include lattice defects such as vacancies [22], dislocations [23,24], and grain boundaries [25]. Among them, grain boundaries are

particularly important, as they influence the overall lattice structure and dynamics.

Grain boundaries are the typical planar lattice defects that form when two crystal grains with different orientations meet during crystal growth. In general, grain boundaries play a crucial role in plastic deformation by hindering or releasing dislocations and affecting their mobility [26,27]. Additionally, grain boundaries behave as a source of other lattice defects [28,29]. As a result, the grain boundaries determine the overall mechanical behavior of polycrystalline materials [26,30]. Furthermore, grain boundaries exhibit lattice mismatches, leading to excess grain boundary energy compared to perfect crystals [31,32]. The local disorder of crystalline arrangement near grain boundaries can be diffusion pathways for vacancies and cause of segregation, making them potential initiation sites for material failure [33–36]. Given these characteristics, grain boundaries and their lattice mismatch significantly impact the overall mechanical properties of crystals, making them an important topic in materials engineering [37,38].

In skyrmion lattices, phenomena such as grain boundary-mediated rotation [23] have been reported, highlighting the importance of grain boundaries from a perspective of lattice mechanics. However, in polar skyrmion lattices, even the fundamental properties, such as structure and stabilization mechanisms of grain boundaries remain unknown. A previous study for dislocation [39] indicated that conventional elasticity theories cannot be applied to polar skyrmion lattices. Instead, a unique “quasiparticle lattice mechanics” emerges from the interaction between skyrmion deformation and lattice distortion. Given this, it is expected that grain boundaries in polar skyrmion lattices possess unique structures and stabilization mechanisms compared to those in atomic crystals.

In this study, we investigate the stable structure of $\Sigma 7$ grain boundaries in polar skyrmion lattices using phase-field

^{*}Contact author: kasai.kohta.72s@st.kyoto-u.ac.jp

[†]Contact author: shimada.takahiro.8u@kyoto-u.ac.jp

simulations. Our results reveal that polar skyrmion grain boundaries undergo transitions into unique structures involving skyrmion deformation depending on electric fields and temperature conditions. Furthermore, through numerical evaluations of lattice and skyrmion deformation, we show a “quasiparticle-based” mismatch relaxation mechanism.

II. SIMULATION METHOD

In general, grain boundary structures in two-dimensional crystals are classified based on the difference between two crystal orientations, often expressed in terms of Σ values, such as $\Sigma 7$ grain boundaries, etc. Although grain boundaries with various tilt angle have been reported [23,25,40], most of them are composed of five–seven pair dislocation skyrmion lattices. In this study, we focus on the $\Sigma 7$ grain boundary structure as a representative configuration of five–seven dislocation arrays and an intrinsically stable structure in polar skyrmion lattices. Polar skyrmions were first observed in a $\text{PbTiO}_3/\text{SrTiO}_3$ superlattice [2], and more recently ferroelectric thin films have emerged as a promising platform exploring for polar skyrmions [17,41,42].

A. Phase-field modeling of ferroelectrics

To investigate the stable structures of polar skyrmion grain boundaries, we perform phase-field simulations of polarization distribution in PbTiO_3 thin film, using polarization $\mathbf{P} = (P_1, P_2, P_3)$ as an order parameter. In ferroelectric systems, the total free-energy density F is written as

$$F = \int_V (f_{\text{Landau}} + f_{\text{grad}} + f_{\text{elect}} + f_{\text{elast}}) dV, \quad (1)$$

where f_{Landau} , f_{grad} , f_{elect} , f_{elast} are the Landau energy density, the gradient energy density, the electrostatic energy density, and elastic energy density, respectively. The Landau energy density, describing the ferroelectric phase transition depending on temperature, is expressed by [43,44]

$$f_{\text{Landau}} = \alpha_{ij} P_i P_j + \alpha_{ijkl} P_i P_j P_k P_l + \alpha_{ijklmn} P_i P_j P_k P_l P_m P_n, \quad (2)$$

where α_{ij} , α_{ijkl} , and α_{ijklmn} are the Landau coefficients. The gradient energy density, describing the formation of polarization domain walls, is expressed by [43]

$$f_{\text{grad}} = \frac{1}{2} G_{ijkl} P_{i,j} P_{k,l}, \quad (3)$$

where G_{ijkl} is the gradient energy coefficient and $P_{i,j} = \frac{\partial P_i}{\partial x_j}$ is the spatial partial derivative of polarization. The electrostatic energy density is expressed by [45]

$$f_{\text{elect}} = -\frac{1}{2} \varepsilon_b E_i E_i - E_i P_i, \quad (4)$$

where ε_b is the background permittivity and E_i is electric field. In this study, screening factor β is introduced to reproduce the electrical boundary conditions of thin-film surface where polar skyrmion appears in the previous study [41]. Thus, the electric field is expressed by

$$E_i = E_i^{\text{ext}} + (1 - \beta) E_i^{\text{dep}}, \quad (5)$$

where E_i^{ext} is external electric field and E_i^{dep} is depolarization field. The elastic energy density is expressed by

$$f_{\text{elast}} = \frac{1}{2} c_{ijkl} \varepsilon_{ij}^{\text{elast}} \varepsilon_{kl}^{\text{elast}}, \quad (6)$$

where c_{ijkl} is the elastic constant and $\varepsilon_{ij}^{\text{elast}}$ is elastic strain. In addition to elastic strain, ferroelectric materials exhibit eigenstrain (intrinsic strain) caused by spontaneous polarization. The eigenstrain ε_{ij}^0 is expressed by [43]

$$\varepsilon_{ij}^0 = Q_{ijkl} P_k P_l, \quad (7)$$

where Q_{ijkl} are electrostrictive coefficients. The total strain ε_{ij} , defined as the displacement gradient in the material, is the sum of elastic strain and eigenstrain and expressed by

$$\varepsilon_{ij}^{\text{elast}} = \varepsilon_{ij} - \varepsilon_{ij}^0. \quad (8)$$

Substituting Eq. (8), f_{elast} is

$$\begin{aligned} f_{\text{elast}} &= \frac{1}{2} c_{ijkl} \varepsilon_{ij}^{\text{elast}} \varepsilon_{kl}^{\text{elast}} = \frac{1}{2} c_{ijkl} (\varepsilon_{ij} - \varepsilon_{ij}^0) (\varepsilon_{kl} - \varepsilon_{kl}^0) \\ &= \frac{1}{2} c_{ijkl} \varepsilon_{ij} \varepsilon_{kl} - \frac{1}{2} c_{ijkl} (\varepsilon_{ij} \varepsilon_{kl}^0 + \varepsilon_{ij}^0 \varepsilon_{kl}) + \frac{1}{2} c_{ijkl} \varepsilon_{ij}^0 \varepsilon_{kl}^0. \end{aligned} \quad (9)$$

Substituting Eq. (7) into the second term, using $c_{ijkl} = c_{klij}$ in for isotropic materials,

$$\begin{aligned} & -\frac{1}{2} c_{ijkl} (\varepsilon_{ij} \varepsilon_{kl}^0 + \varepsilon_{ij}^0 \varepsilon_{kl}) \\ &= -\frac{1}{2} c_{ijkl} (\varepsilon_{ij} Q_{klmn} P_m P_n + Q_{ijmn} P_m P_n \varepsilon_{kl}) \\ &= -\frac{1}{2} (c_{ijmn} + c_{mnij}) Q_{mnkl} \varepsilon_{ij} P_k P_l \\ &= -c_{ijmn} Q_{mnkl} \varepsilon_{ij} P_k P_l = -q_{ijkl} \varepsilon_{ij} P_k P_l, \end{aligned} \quad (10)$$

where $q_{ijkl} (= c_{ijmn} Q_{mnkl})$ are piezoelectric coupling coefficients. And the third term is

$$\begin{aligned} \frac{1}{2} c_{ijkl} \varepsilon_{ij}^0 \varepsilon_{kl}^0 &= \frac{1}{2} c_{ijkl} Q_{ijmn} P_m P_n Q_{klmn} P_m P_n \\ &= \frac{1}{2} c_{mnop} Q_{mnij} Q_{opkl} P_i P_j P_k P_l. \end{aligned} \quad (11)$$

The right side of this equation is the fourth-order term of P_i , which can be incorporated into Landau energy density. Therefore, f_{elast} is expressed by

$$f_{\text{elast}} = \frac{1}{2} c_{ijkl} \varepsilon_{ij} \varepsilon_{kl} - q_{ijkl} \varepsilon_{ij} P_k P_l. \quad (12)$$

The second term of Eq. (9) describes the piezoelectric coupling effect in ferroelectric materials.

The governing equations of the phase-field simulation consist of the time-dependent Ginzburg-Landau (TDGL) equation, mechanical equilibrium equation, and Maxwell's equation. The TDGL equation is written as

$$\partial P_i / \partial t = -L (\delta F / \delta P_i), \quad (13)$$

where t is time, L is the kinetic coefficient, and $F = \int f_{\text{total}} dV$ is total free energy of the system. The mechanical equilibrium equation is

$$\sigma_{ij,j} = (\partial f / \partial \varepsilon_{ij})_{,j} = 0, \quad (14)$$

where $\sigma_{ij,j}$ is the stress gradient. Maxwell's equation is

$$D_{i,i} = (-\partial f / \partial E_i)_{,i} = 0, \quad (15)$$

where $D_{i,i}$ is the electric displacement gradient in the material. Equations (13)–(15) are the governing equations of the phase-field simulation.

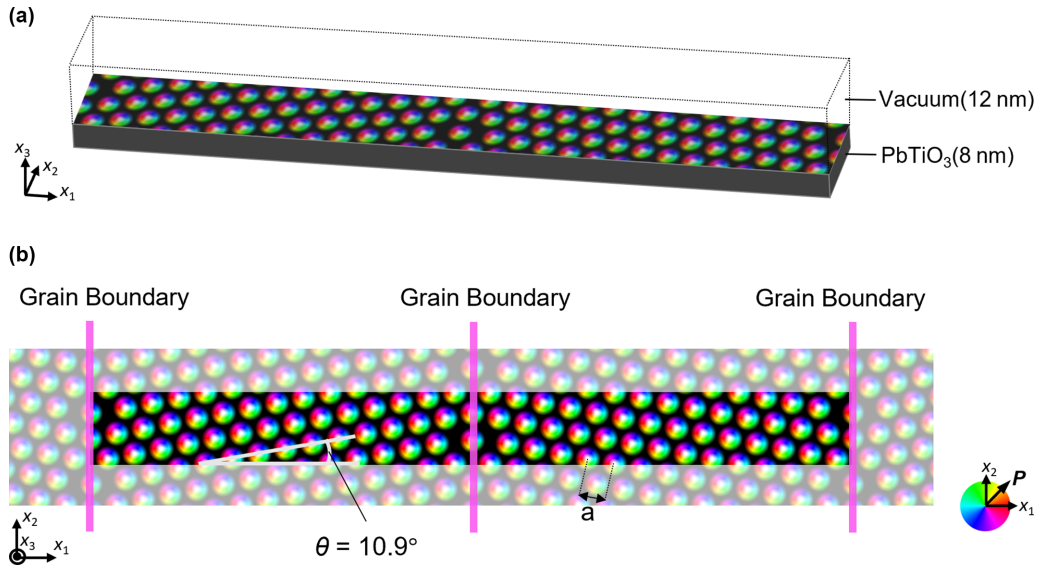


FIG. 1. Schematic of simulation model in (a) 3D view and (b) 2D view. The pink lines represent the positions of the skyrmion grain boundaries. Light-colored areas represent the image cells under periodic boundary conditions.

B. Simulation model and procedure

As shown in Fig. 1(a), the simulation model consists of an 8-nm-thick PbTiO₃ film and a 12-nm vacuum layer in the x_3 direction. Assuming the presence of a substrate, a -1% misfit strain is applied to the PbTiO₃ film. The screening factor is set to $\beta = 0.2$. These external factors are selected to ensure that skyrmion phase remains stable over a wide range of temperatures and electric fields based on a previous study [41], enabling investigation of grain boundary structures depending on quasiparticle features of skyrmion. The initial polarization distribution in PbTiO₃ film forms two perfect hexagonal skyrmion lattices with different orientations, each having a lattice constant $a(E, T)$, as listed in Tables S1 and S2 in the Supplemental Material [53]. The lattice is tilted by $\theta (= 10.9^\circ)$ in the left half of the simulation model and $-\theta$ in the right half, creating a lattice mismatch corresponding to a $\Sigma 7$ grain boundary at the center and the edge of the model under three-dimensional (3D) periodic boundary conditions [Fig. 1(b)]. The $\Sigma 7$ grain boundary structure, characterized by straightly aligned dislocations and commonly observed in magnetic skyrmion lattices, is adopted as the reference structure in this study. To minimize interactions between grain boundaries, we decided on the model size and initial polarization distribution so that 14 skyrmions aligned between the grain boundaries. To account for the free volume of grain boundaries, multiple simulations were performed by varying the model length in the x_1 direction, and the most stable grain boundary structure with the lowest total free energy was determined. The model length in the x_2 direction is set to match the repeating units under periodical boundary conditions. As a result, the actual model lengths in x_1 and x_2 directions are $(l_1, l_2) = (388.6 \text{ nm}, 38.5 \text{ nm}), (416.1 \text{ nm}, 39.7 \text{ nm}),$ and $(436.3 \text{ nm}, 41.0 \text{ nm})$ for $E = 12, 9,$ and 6 MV/cm , respectively. The entire simulation model is divided into grids of approximately 1 nm width. All of the material parameters used in this study are listed in Table S3 [53]. Equations (13)–(15) are numerically

solved using semi-implicit Fourier-spectral method [46,47] and Fourier spectral iterative perturbation method [48,49], under varied out-of-plane electric field and temperature conditions. This method has been successfully used in previous studies to reproduce the emergence of polar skyrmions and skyrmion lattices [39,50].

III. RESULTS

A. Skyrmion grain boundary structure under high electric field (12 MV/cm)

Figures 2(a-1), 2(b-1), and 2(c-1) illustrate the three-dimensional polarization structures near the skyrmion grain boundary under electric fields of $E = 12, 9,$ and 6 MV/cm , respectively. These figures show that regions with downward out-of-plane polarization exist within a surrounding upward out-of-plane region, with in-plane polarization at the intermediate transitions. Notably, near the upper surface, the polarization vectors continuously converge toward the skyrmion center, while near the lower surface, they diverge outward. This three-dimensional polar structure is characteristic of a skyrmion bubble, previously observed in PbTiO₃/SrTiO₃ superlattices [2]. In addition, the skyrmions have Néel-type domain wall, consistent with other theoretical and experimental studies [17,41,51]. As shown in Fig. 2(a-2), under a high electric field ($E = 12 \text{ MV/cm}$), each skyrmion has circular shape without significant deformation, with an approximate diameter of 10 nm. At the grain boundary, fivefold and sevenfold coordinated skyrmions are present and are arranged parallel to the grain boundary plane. This configuration is structurally analogous to a conventional $\Sigma 7$ grain boundary, where five–seven pairs align sequentially. A notable aspect of this result is that the vector order polar skyrmions behave as discrete particles, forming a grain boundary structure similar to that observed in atomic crystals. To characterize the topological nature of the skyrmions, we calculated the Pontryagin

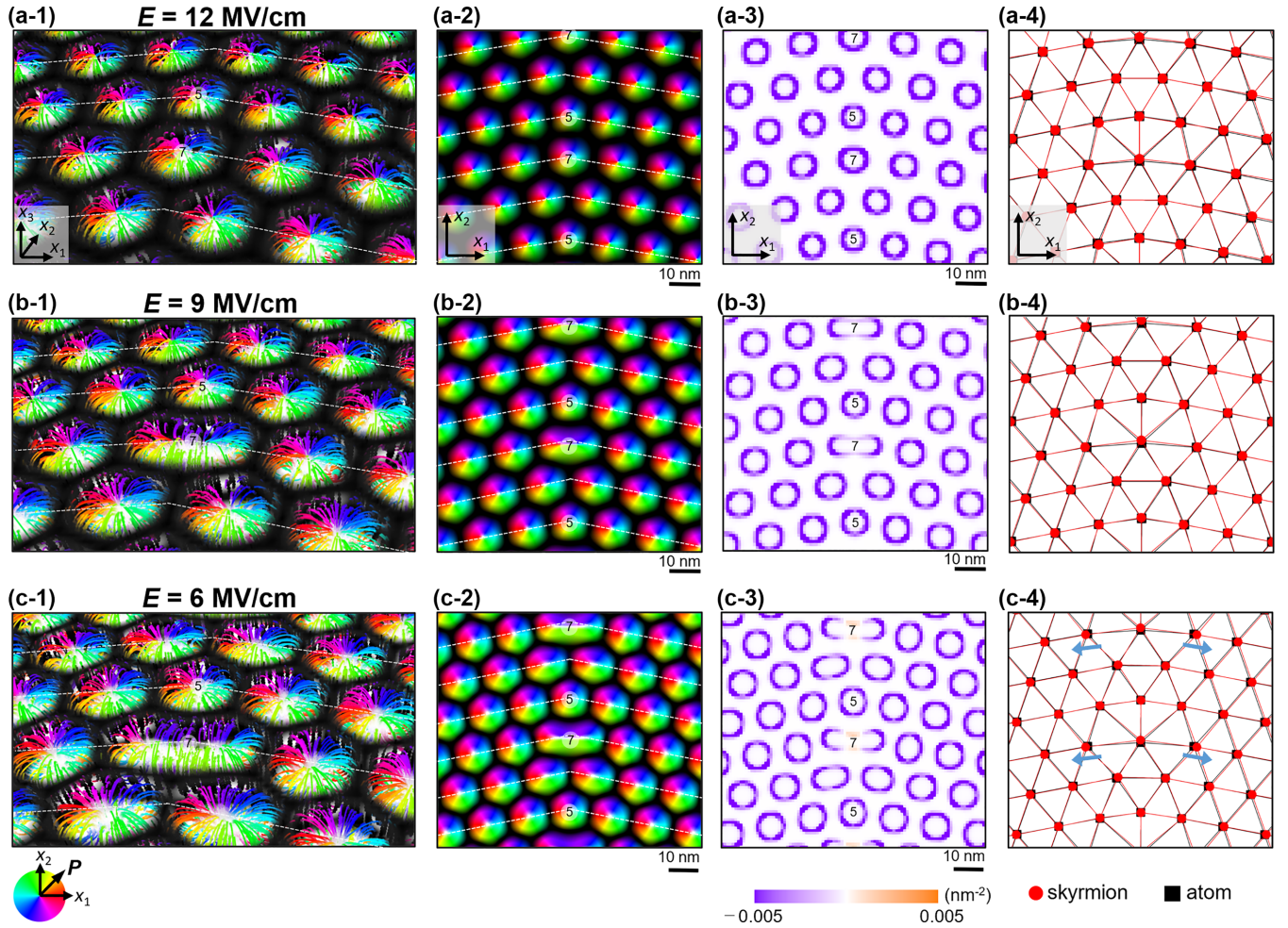


FIG. 2. Three-dimensional view (a-1)–(c-1) and two-dimensional view (a-2)–(c-2) of polarization distribution at the skyrmion grain boundaries. (a-3)–(c-3) Pontryagin charge density near the skyrmion grain boundaries. (a-4)–(c-4) Differences in the positions of lattice points between the skyrmion grain boundaries and an atomic grain boundary. The length scales are normalized by lattice constants. In (a)–(c), the external out-of-plane electric field is $E = 12, 9$, and 6 MV/cm, respectively.

charge density [52] q ,

$$q = \frac{1}{4\pi} \int_S \mathbf{P} \cdot \left(\frac{\partial \mathbf{P}}{\partial x} \times \frac{\partial \mathbf{P}}{\partial y} \right) d^2r, \quad (16)$$

where \mathbf{P} is the normalized polarization vector, and its distribution is shown in Fig. 2(a-3). The negative q values form a ring-based pattern around the outer edges of each skyrmion, consistent with previous studies [2] on polar skyrmions. The same distribution is found for other skyrmions, indicating that they are topologically equivalent. Furthermore, to compare the lattice characteristics of this skyrmion grain boundary with those of atomic crystals, Fig. 2(a-4) presents a comparison between individual skyrmion positions and atomic positions obtained from molecular statics (MS) simulations of an atomic grain boundary (see Supplemental Material [53]). With only minor exceptions, the lattice points in both structures align closely, confirming that the arrangement of skyrmions within the skyrmion grain boundary closely resembles that of atoms in an atomic crystal. Therefore, under high electric field conditions, circular skyrmions form a grain

boundary structure analogous to that observed in atomic crystals.

B. Skyrmion grain boundary structure under medium electric field (9 MV/cm)

Under a medium electric field ($E = 9$ MV/cm), as shown in Fig. 2(b-2), the sevenfold skyrmion elongates in the x_1 direction, while other skyrmions retain their circular shape. The major axis of the sevenfold skyrmion measures 18 nm, approximately two times that of other skyrmions. This corresponds to the fact that the sevenfold lattice points accommodate a larger area within the lattice mismatch region at the grain boundary. Similar elongation of sevenfold skyrmions has also been observed in magnetic skyrmions at grain boundaries [25]. From the topological charge distribution shown in Fig. 2(b-3), a ring-based negative q distribution appears in correspondence with the elongation of the sevenfold skyrmion. This characteristic is similar to that of circular skyrmions, indicating that the topological properties remain equivalent. Furthermore, as shown in Fig. 2(b-4), the skyrmion arrangement aligns closely with that of atomic crystals, similar to

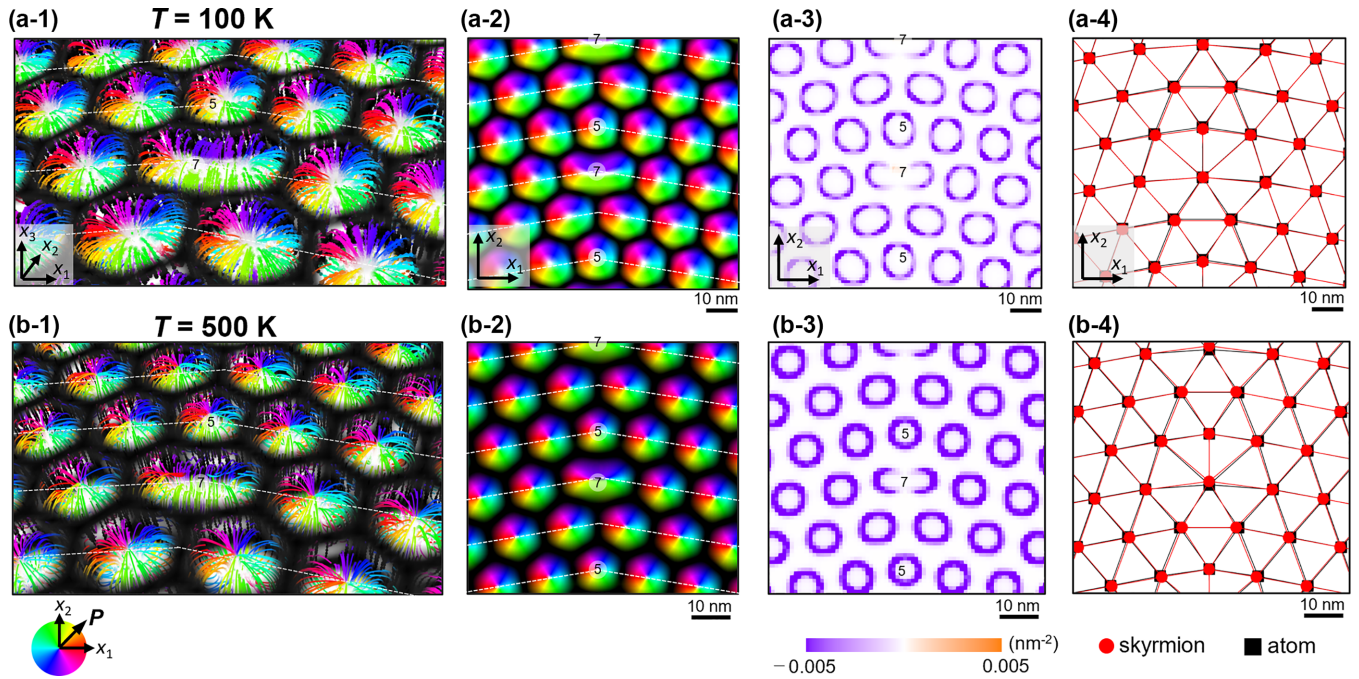


FIG. 3. Three-dimensional view (a-1), (b-1) and two-dimensional view (a-2), (b-2) of polarization distribution at the skyrmion grain boundaries. (a-3), (b-3) Pontryagin charge density near the skyrmion grain boundaries. (a-4), (b-4) Differences in the positions of lattice points between the skyrmion grain boundaries and an atomic grain boundary. The length scales are normalized by lattice constants. In (a) and (b), the temperature is $T = 100$ and 500 K.

the high-field case, with no significant deviations in lattice point positioning at the grain boundary. Note that the grain boundary free volume change of skyrmion lattice is taken into account in the atomic arrangements. Therefore, under medium electric field conditions, even the sevenfold skyrmion undergoes elongation, and the grain boundary structure remains analogous to that in atomic crystals.

C. Skyrmion grain boundary structure under low electric field (6 MV/cm)

On the other hand, as shown in Fig. 2(c-2), under a low electric field ($E = 6$ MV/cm), skyrmion deformations at the grain boundary become significant. Notably, the sevenfold skyrmion is highly elongated in the x_1 direction, and the two skyrmions positioned below the sevenfold skyrmion are also stretched. In contrast, circular skyrmions are distributed in regions away from the grain boundary, suggesting that skyrmion deformation is induced by lattice mismatch at the grain boundary. Even in these elongated skyrmions, as shown in Fig. 2(c-3), the topological charge q remains distributed along their outer edges. However, unlike other skyrmions, the sevenfold skyrmion exhibits non-negative values in its intermediate section. This indicates that the middle part of the sevenfold skyrmion formed by the elongation has a polarization structure similar to the stripe phase. In other words, a local topological transition occurs in the highly elongated sevenfold skyrmion. Furthermore, as shown in Fig. 2(c-4), despite the large skyrmion deformations, the arrangement of skyrmions almost remains aligned with the atomic grain boundary. However, only the skyrmions beside the sevenfold skyrmion are slightly shifted in the x_1 direction, consistent

with the deformation direction of the sevenfold skyrmion. These observations indicate that under low electric fields, although some skyrmions significantly deform with topological transitions, the fundamental grain boundary structure remains consistent with that of atoms, except in the vicinity of the most deformed skyrmion, the sevenfold skyrmion.

Based on these findings, in skyrmion grain boundaries (GBs), although individual skyrmions exhibit electric-field-dependent deformation, the overall structural characteristics remain largely unchanged. Under high electric fields, the skyrmion GB consists of rigid circular skyrmions, whereas the sevenfold skyrmion deforms significantly as the electric field decreases. The arrangement of each skyrmion is similar to that of an atomic grain boundary, however, in the vicinity of the highly deformed sevenfold skyrmion, slight positional shifts of adjacent skyrmions occur.

D. Temperature dependence of skyrmion grain boundary structure

We also investigate the temperature dependence of polar skyrmion grain boundaries. Figure 3 presents the skyrmion grain boundaries at an electric field of $E = 6$ MV/cm and temperatures of $T = 100$ and 500 K. At $T = 100$ K, as shown in Figs. 3(a-1) and 3(a-2), the skyrmions are generally large and exhibit significant deformation near the grain boundary, similar to the distribution observed at $T = 300$ K. The topological charge density [Fig. 3(a-3)] shows positive values at sevenfold skyrmion, indicating the topological phase transition. In contrast, at $T = 500$ K, as shown in Figs. 3(b-1) and 3(b-2), individual skyrmions are relatively smaller with less deformation. The magnitude of polarization values

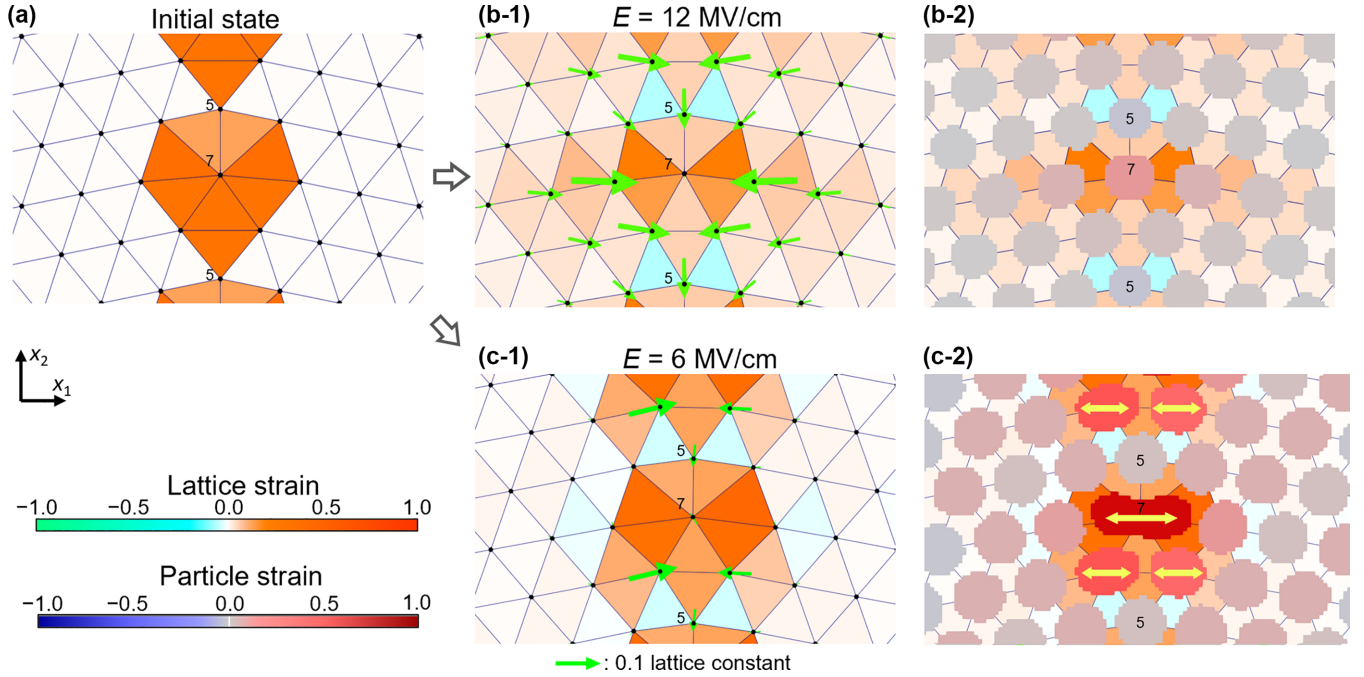


FIG. 4. Distributions of lattice strain in the x_1 direction near the skyrmion grain boundaries at (a) initial configurations and (b-1), (c-1) equilibrium state of $E = 12$ and 6 MV/cm. The size and directions of the green arrows represent the displacements of each skyrmion from the initial configurations. (b-2), (c-2) The particle strains (rate of change in the long axis) are shown by the color of skyrmion particles. The yellow arrows indicate skyrmions with substantial deformation.

$|P| = \sqrt{P_1^2 + P_2^2 + P_3^2}$ range from 0.145 to 0.448 C/m² at $T = 100$ K, 0.058 to 0.329 C/m² at $T = 300$ K, and 0.014 to 0.193 C/m² at $T = 500$ K. This indicates that polarization increases as temperature decreases, which can be attributed to the temperature dependence of polarization described by the Landau energy [Eq. (2)]. Additionally, as shown in Figs. 3(a-4) and 3(b-4), the positions of each skyrmion consist with atomic grain boundary in both temperature conditions. Overall, at lower temperatures, both the skyrmion size and deformation increase, whereas at higher temperatures, they decrease. Although this trend is less pronounced than the changes induced by variations in the electric field, it follows a similar pattern. This behavior can be explained by the fact that at lower temperatures, the absolute polarization is larger, making the relative influence of the electric field smaller, while at higher temperatures, the absolute polarization is smaller, making the relative influence of the electric field larger.

IV. DISCUSSIONS

A. Quasiparticle-based relaxation mechanism in skyrmion grain boundaries

It is essential to discuss the characteristics of skyrmion grain boundaries from the perspective of lattice mechanics. In general, grain boundaries represent regions of lattice mismatch, and their relaxation plays a crucial role in determining the crystal structure, mechanical strength, and other material properties. Therefore, understanding the mechanism by which skyrmion grain boundaries relax lattice mismatches is important. Here, we use the lattice strain [39,57] in skyrmion lattices as an indicator of lattice mismatch. To quantify this, we construct triangular lattice by treating the center points of

each skyrmion as a lattice point and applying Delaunay triangulation. The local lattice strain is then calculated for each triangle by comparing it with an ideal equilateral triangle from a reference perfect lattice. Figure 4 shows the lattice strain distribution of skyrmion GBs at the initial state and the equilibrium states under electric fields of $E = 12$ and 6 MV/cm. At the initial configuration, as shown in Fig. 4(a), skyrmions are regularly arranged, and locally high lattice strain appears only at the grain boundary region, while the rest of the lattice remains strain free, similar to a perfect crystal. This indicates that the lattice mismatch is localized exclusively at the grain boundary region.

In contrast, at the equilibrium state under $E = 12$ MV/cm, as shown in Fig. 4(b-1), strains are also distributed in the lattices near the grain boundary. While the lattice strain at the grain boundary itself has decreased compared to the initial state, previously unstrained surrounding lattices now exhibit positive strain values, with higher values observed closer to the boundary. Additionally, as indicated by the green arrows in the figure, skyrmions near the grain boundary have moved significantly. These indicate that the position changes of skyrmions around the grain boundary disperse the local lattice strain from the boundary into the surrounding lattices, thereby relaxing the localized geometric mismatch of the grain boundary. Furthermore, as shown in Fig. 4(b-2), individual skyrmions remain undeformed, with the most deformed sevenfold skyrmion exhibiting only 15% deformation. This indicates that skyrmion deformation does not contribute to this relaxation process. Thus, under high electric field conditions, we confirm a lattice-stabilization mechanism similar to that in atomic crystals, where the geometric mismatch at the grain boundary is alleviated by the movement of nearby skyrmions.

TABLE I. Grain boundary energy and grain boundary free volume of skyrmion grain boundaries under various electric field conditions with temperature $T = 300$ K.

E (MV/cm)	6	9	12
Grain boundary energy (10^{-11} J/m)	-1.31	-1.015	4.140
Grain boundary free volume	0.124	0.048	-0.149

On the other hand, under the lower electric field condition ($E = 6$ MV/cm), as shown in Fig. 4(c-1), the high lattice strain at the grain boundary remains even in the equilibrium state. In particular, the strain in the lattice containing the sevenfold skyrmion remains almost unchanged from the initial state. Additionally, except for a few lattice points, the skyrmions have not moved significantly, indicating that the mismatch relaxation by skyrmion arrangement observed under higher electric field conditions does not occur under low electric field conditions. Furthermore, as shown in Fig. 4(c-2), the deformation of skyrmions at the grain boundary is significantly larger, with the most pronounced deformation occurring in the sevenfold skyrmion at 94%, followed by the skyrmions below it at 24%. Therefore, the surrounding skyrmions in regions of high lattice strain exhibit substantial deformation. In addition, as shown in Fig. S1 [53], the lattice strain in the x_2 direction is significantly smaller than that in the x_1 direction, highlighting the strong correspondence between lattice strain and skyrmion deformation. These results indicate that under low electric field conditions, the maintenance of lattice mismatches by skyrmion deformations takes place instead of the relaxation of mismatches through skyrmion arrangement. This is a quasiparticle-based stabilization mechanism unique to skyrmions, which is fundamentally different from conventional lattice behavior. Moreover, we also investigated a zigzag grain boundary structure shown in Fig. S2 [53] and confirmed that similar stabilization mechanisms apply even in asymmetric configurations, suggesting the generality of the revealed mechanism. Therefore, the stabilization mechanisms of grain boundaries in skyrmion lattices transitions from lattice mechanism with skyrmion arrangements to quasiparticle mechanism with skyrmion deformations depending on the electric field.

B. Energetic and structural characteristics of skyrmion grain boundaries

To systematically characterize the skyrmion grain boundaries, we calculated two fundamental attributes of grain boundaries, grain boundary free volume (BFV) [58,59] and grain boundary energy (GBE) [31,60,61], under various conditions. BFV is the excess volume compared to the perfect lattice due to the presence of grain boundaries and usually evaluated as an excess volume per unit grain boundary surface. GBE is excess free energy due to existence of grain boundaries, and also evaluated as values per grain boundary surface. To calculate these values, additional simulations of the perfect crystal model without grain boundaries were performed. Since the skyrmion lattice is a two-dimensional crystal, both BFV and GBE here are calculated as values per

TABLE II. Grain boundary energy and grain boundary free volume of skyrmion grain boundaries with various temperature conditions under external electric field $E = 6$ MV/cm.

T (K)	100	300	500
Grain boundary energy (10^{-11} J/m)	-6.61	-1.31	-6.75
Grain boundary free volume	0.134	0.124	0.113

grain boundary length. BFV δ is expressed as

$$\delta = \frac{l_x^{\text{GB}} - l_x^{\text{PL}}}{2l_y}, \quad (17)$$

where l_x^{GB} and l_x^{PL} are model length in the x_1 direction of grain boundary model and perfect lattice model, and l_y is the model length in the x_2 direction. GBE γ is expressed as

$$\gamma = \frac{F^{\text{GB}} - F^{\text{PL}}}{2l_y}, \quad (18)$$

where F^{GB} and F^{PL} are total free energy of grain boundary model and perfect lattice model. Table I presents the calculated values, indicating that as the electric field increases, the GBE increases while BFV decreases. A similar trend is observed with increasing temperature, shown in Table II. In other words, under low electric field and low temperature conditions, where skyrmion deformation is more pronounced, BFV is larger and GBE is lower. Notably, at $E = 6$ and 9 MV/cm, GBEs are negative. Although GBEs are generally positive in atomic crystals, previous studies have reported cases of negative defect formation energies under specific materials or external conditions [62,63], indicating that defect structures can form spontaneously. Therefore, the negative GBEs in skyrmion lattice suggest that decreasing electric field may lead to spontaneous grain boundary formation. In typical atomic crystals, GBE primarily arises from elastic energy due to atomic displacements. However, in skyrmion crystals, mismatch relaxation is not only governed by skyrmion movement but also by skyrmion deformation. This additional degree of freedom allows for a reduction in GBE, highlighting a distinct stabilization mechanism based on quasiparticle deformation, which is fundamentally different from classical grain boundary behavior.

V. CONCLUSION

In summary, this study demonstrates that the grain boundaries of polar skyrmions undergo structural transitions from atomic-based configurations to unique skyrmion-specific structures depending on electric field and temperature, accompanied by changes in their stabilization mechanisms. Under high electric fields and high temperature conditions, skyrmions have circular shape and form grain boundary structures similar to those in atomic crystals. In this structure, the skyrmions near the grain boundaries adjust their positions to relax the lattice mismatches. In contrast, under low electric fields and low-temperature conditions, skyrmions at the grain boundary undergo significant deformation, maintaining large local lattice mismatches. This indicates a quasiparticle-based stabilization mechanism distinct from conventional

crystals. Generally, in atomic crystal growth, atoms arrange themselves to minimize grain boundary mismatches, influencing the final crystal structure, mechanical strength, and other material properties [64]. The unique structures and stabilization mechanisms observed in polar skyrmion grain boundaries indicate the distinctive lattice dynamics of polar skyrmion lattices due to the grain boundary properties and suggest the potential emergence of novel electromechanical properties. Furthermore, the transition in stabilization mechanisms, from lattice relaxation via skyrmion arrangement to quasiparticle stabilization through skyrmion deformation, identified in this study may also be relevant to the growth process of polar skyrmion lattices and their response to macroscopic external forces. Therefore, our findings provide fundamental insights into the general stabilization mechanisms of polar skyrmion lattices.

During the preparation of this work, the authors used ChatGPT in order to proofread the manuscript and improve the wording. After using this tool, the authors reviewed and edited the content as needed and take full responsibility for the content of the publication.

ACKNOWLEDGMENT

This work was supported by JSPS KAKENHI (Grants No. JP23H00159, No. JP23K17720, and No. JP24H00032), JST FOREST Program (Grant No. JPMJFR222H), and JSPS SPRING (Grant No. JPMJSP2110).

K.K. performed the phase-field simulations, analyzed the data, and wrote the manuscript. S. Miyata performed the phase-field simulations. S. Minami provided critical feedback on the manuscript. T.S. conceived the project and supervised the work. All authors contributed to the general discussion and comment on the manuscript.

DATA AVAILABILITY

The data that support the findings of this article are not publicly available upon publication because it is not technically feasible and/or the cost of preparing, depositing, and hosting the data would be prohibitive within the terms of this research project. The data are available from the authors upon reasonable request.

- [1] Y. Nahas, S. Prokhorenko, L. Louis, Z. Gui, I. Kornev, and L. Bellaiche, Discovery of stable skyrmionic state in ferroelectric nanocomposites, *Nat. Commun.* **6**, 8542 (2015).
- [2] S. Das, Y. L. tang, Z. Hong, M. A. P. Gonçalves, M. R. McCarter, C. Klewe, K. X. Nguyen, F. Gómez-Ortiz, P. Shafer, E. Arenholz *et al.*, Observation of room-temperature polar skyrmions, *Nature (London)* **568**, 368 (2019).
- [3] S. Mühlbauer, B. Binz, F. Jonietz, C. Pfleiderer, A. Rosch, A. Neubauer, R. Georgii, and P. Böni, Skyrmion lattice in a chiral magnet, *Science* **323**, 915 (2009).
- [4] X. Z. Yu, Y. Onose, N. Kanazawa, J. H. Park, J. H. Han, Y. Matsui, N. Nagaosa, and Y. Tokura, Real-space observation of a two-dimensional skyrmion crystal, *Nature (London)* **465**, 901 (2010).
- [5] H. Ge, X.-Y. Xu, L. Liu, R. Xu, Z.-K. Lin, S.-Y. Yu, M. Bao, J.-H. Jiang, M.-H. Lu, and Y.-F. Chen, Observation of acoustic skyrmions, *Phys. Rev. Lett.* **127**, 144502 (2021).
- [6] C. Liu, S. Zhang, S. A. Maier, and H. Ren, Disorder-induced topological state transition in the optical skyrmion family, *Phys. Rev. Lett.* **129**, 267401 (2022).
- [7] J. Sampaio, V. Cros, S. Rohart, A. Thiaville, and A. Fert, Nucleation, stability and current-induced motion of isolated magnetic skyrmions in nanostructures, *Nat. Nanotechnol.* **8**, 839 (2013).
- [8] A. Neubauer, C. Pfleiderer, B. Binz, A. Rosch, R. Ritz, P. G. Niklowitz, and P. Böni, Topological hall effect in the a phase of MnSi, *Phys. Rev. Lett.* **102**, 186602 (2009).
- [9] A. Fert, V. Cros, and J. Sampaio, Skyrmions on the track, *Nat. Nanotechnol.* **8**, 152 (2013).
- [10] X. Zhang, M. Ezawa, and Y. Zhou, Magnetic skyrmion logic gates: conversion, duplication and merging of skyrmions, *Sci. Rep.* **5**, 9400 (2015).
- [11] H. Zhang, D. Zhu, W. Kang, Y. Zhang, and W. Zhao, Stochastic computing implemented by skyrmionic logic devices, *Phys. Rev. Appl.* **13**, 054049 (2020).
- [12] M.-K. Lee and M. Mochizuki, Handwritten digit recognition by spin waves in a Skyrmion reservoir, *Sci. Rep.* **13**, 19423 (2023).
- [13] T. Yokouchi, S. Sugimoto, B. Rana, S. Seki, N. Ogawa, Y. Shiomi, S. Kasai, and Y. Otani, Pattern recognition with neuromorphic computing using magnetic field-induced dynamics of skyrmions, *Sci. Adv.* **8**, eabq5652 (2022).
- [14] H. Aramberri and J. Íñiguez-González, Brownian electric bubble quasiparticles, *Phys. Rev. Lett.* **132**, 136801 (2024).
- [15] M. A. P. Gonçalves, M. Paściak, and J. Hlinka, Antiskyrmions in ferroelectric barium titanate, *Phys. Rev. Lett.* **133**, 066802 (2024).
- [16] M. A. Pereira Gonçalves, C. Escorihuela-Sayalero, P. García-Fernández, J. Junquera, and J. Íñiguez, Theoretical guidelines to create and tune electric skyrmion bubbles, *Sci. Adv.* **5**, (2019).
- [17] L. Han *et al.*, High-density switchable skyrmion-like polar nanodomains integrated on silicon, *Nature (London)* **603**, 63 (2022).
- [18] S. Das *et al.*, Local negative permittivity and topological phase transition in polar skyrmions, *Nat. Mater.* **20**, 194 (2021).
- [19] L. Gao, S. Prokhorenko, Y. Nahas, and L. Bellaiche, Dynamical control of topology in polar skyrmions via twisted light, *Phys. Rev. Lett.* **132**, 026902 (2024).
- [20] Y.-T. Shao *et al.*, Emergent chirality in a polar meron to skyrmion phase transition, *Nat. Commun.* **14**, 1355 (2023).
- [21] J. Ren, L. Liu, F. Sun, Q. He, M. Wu, W. Chen, and Y. Zheng, Emergence and transformation of polar skyrmion lattices via flexoelectricity, *npj Computat. Mater.* **10**, 216 (2024).
- [22] X. Yu, D. Morikawa, T. Yokouchi, K. Shibata, N. Kanazawa, F. Kagawa, T. Arima, and Y. Tokura, Aggregation and collapse dynamics of skyrmions in a non-equilibrium state, *Nat. Phys.* **14**, 832 (2018).
- [23] S. Pöllath *et al.*, Dynamical defects in rotating magnetic skyrmion lattices, *Phys. Rev. Lett.* **118**, 207205 (2017).
- [24] R. Brearton, M. W. Olszewski, S. Zhang, M. R. Eskildsen, C. Reichhardt, C. J. O. Reichhardt, G. Van Der Laan, and T. Hesjedal, Skyrmions in anisotropic magnetic fields: Strain and defect driven dynamics, *MRS Adv.* **4**, 643 (2019).

- [25] T. Matsumoto, Y.-G. So, Y. Kohno, H. Sawada, Y. Ikuhara, and N. Shibata, Direct observation of $\Sigma 7$ domain boundary core structure in magnetic skyrmion lattice, *Sci. Adv.* **2**, e1501280 (2016).
- [26] J. P. Hirth, The influence of grain boundaries on mechanical properties, *Metall. Trans.* **3**, 3047 (1972).
- [27] J. Kacher, B. P. Eftink, B. Cui, and I. M. Robertson, Dislocation interactions with grain boundaries, *Curr. Opin. Solid State Mater. Sci.* **18**, 227 (2014).
- [28] M. Upmanyu, D. J. Srolovitz, L. S. Shvindlerman, and G. Gottstein, Vacancy generation during grain boundary migration, *Interface Sci.* **6**, 289 (1998).
- [29] H. Gleiter, Grain boundaries as point defect sources or sinks—Diffusional creep, *Acta Metall.* **27**, 187 (1979).
- [30] Z. Gong, W. Zhao, K. Guan, P. Rao, Q. Zeng, J. Liu, and Z. Feng, Influence of grain boundary and grain size on the mechanical properties of polycrystalline ceramics: Grain-scale simulations, *J. Am. Ceram. Soc.* **103**, 5900 (2020).
- [31] M. E. Glicksman and R. A. Masumura, Grain boundary structure and energetics, *Metall. Trans. A* **8**, 1373 (1977).
- [32] T. Uesugi and K. Higashi, First-principles calculation of grain boundary excess volume and free volume in nanocrystalline and ultrafine-grained aluminum, *Mater. Trans.* **54**, 1597 (2013).
- [33] R. E. Hoffman and D. Turnbull, Lattice and grain boundary self-diffusion in silver, *J. Appl. Phys.* **22**, 634 (1951).
- [34] J. C. Fisher, Calculation of diffusion penetration curves for surface and grain boundary diffusion, *J. Appl. Phys.* **22**, 74 (1951).
- [35] M. P. Seah, Grain boundary segregation, *J. Phys. F: Met. Phys.* **10**, 1043 (1980).
- [36] M. D. Sangid, H. J. Maier, and H. Sehitoglu, The role of grain boundaries on fatigue crack initiation—An energy approach, *Int. J. Plast.* **27**, 801 (2011).
- [37] T. Watanabe, The impact of grain boundary character distribution on fracture in polycrystals, *Mater. Sci. Eng.* **176**, 39 (1994).
- [38] A. Das, Grain boundary engineering: fatigue fracture, *Philos. Mag.* **97**, 867 (2017).
- [39] K. Kasai, T. Xu, S. Minami, and T. Shimada, Breakdown of volterra's elasticity theory of dislocations in polar skyrmion lattices, *Nano Lett.* **24**, 13247 (2024).
- [40] X. Fang, V. Viteri-Pflucker, A. H. King, J. Wang, J. Yan, L. Ke, and L. Zhou, Oscillating grain boundaries and their effects on grain growth: Observations in skyrmion bicrystals, *Acta Mater.* **290**, 120965 (2025).
- [41] S. Yuan, Z. Chen, S. Prokhorenko, Y. Nahas, L. Bellaiche, C. Liu, B. Xu, L. Chen, S. Das, and L. W. Martin, Hexagonal close-packed skyrmion lattice in ultrathin ferroelectric PbTiO_3 films, *Phys. Rev. Lett.* **130**, 226801 (2023).
- [42] X. Zhang *et al.*, Creation and erasure of polar bubble domains in PbTiO_3 films by mechanical stress and light illuminations, *J. Materiomics* **9**, 626 (2023).
- [43] Y. L. Li, S. Y. Hu, Z. K. Liu, and L. Q. Chen, Effect of substrate constraint on the stability and evolution of ferroelectric domain structures in thin films, *Acta Mater.* **50**, 395 (2002).
- [44] G. Sheng, Y. L. Li, J. X. Zhang, S. Choudhury, Q. X. Jia, V. Gopalan, D. G. Schlom, Z. K. Liu, and L. Q. Chen, A modified Landau–Devonshire thermodynamic potential for strontium titanate, *Appl. Phys. Lett.* **96**, 232902 (2010).
- [45] C. H. Woo and Y. Zheng, Depolarization in modeling nano-scale ferroelectrics using the Landau free energy functional, *Appl. Phys. A* **91**, 59 (2008).
- [46] L. Q. Chen and J. Shen, Applications of semi-implicit Fourier-spectral method to phase field equations, *Comput. Phys. Commun.* **108**, 147 (1998).
- [47] H.-L. Hu and L.-Q. Chen, Three-dimensional computer simulation of ferroelectric domain formation, *J. Am. Ceram. Soc.* **81**, 492 (2005).
- [48] J. J. Wang, S. Bhattacharyya, Q. Li, T. W. Heo, X. Q. Ma, and L.-Q. Chen, Elastic solutions with arbitrary elastic inhomogeneity and anisotropy, *Philos. Mag. Lett.* **92**, 327 (2012).
- [49] J. J. Wang, X. Q. Ma, Q. Li, J. Britson, and L.-Q. Chen, Phase transitions and domain structures of ferroelectric nanoparticles: Phase field model incorporating strong elastic and dielectric inhomogeneity, *Acta Mater.* **61**, 7591 (2013).
- [50] K. Kasai, T. Itano, S. Minami, and T. Shimada, Microscopic formation process of polar skyrmions and strain-dependent topological phase transitions in $\text{PbTiO}_3/\text{SrTiO}_3$ superlattices, *Scripta Mater.* **263**, 116680 (2025).
- [51] Y. Zhang, Q. Li, H. Huang, J. Hong, and X. Wang, Strain manipulation of ferroelectric skyrmion bubbles in a freestanding PbTiO_3 film: A phase field simulation, *Phys. Rev. B* **105**, 224101 (2022).
- [52] N. Nagaosa and Y. Tokura, Topological properties and dynamics of magnetic skyrmions, *Nat. Nanotechnol.* **8**, 899 (2013).
- [53] See Supplemental Material at <http://link.aps.org/supplemental/10.1103/xk7g-v1c7> for details of molecular statics simulation for comparison with skyrmion systems in Fig. 2. The Supplemental Material also contains Refs. [54–56].
- [54] Y. Gu, M. Li, A. N. Morozovska, Y. Wang, E. A. Eliseev, V. Gopalan, and L.-Q. Chen, Flexoelectricity and ferroelectric domain wall structures: Phase-field modeling and DFT calculations, *Phys. Rev. B* **89**, 174111 (2014).
- [55] L. Jiang, J. Tang, Y. Zhou, Q. Yang, Y. Zhang, L. Guo, and X. Zhong, Simulations of local-mechanical-stress-induced ferroelectric polarization switching by a multi-field coupling model of flexoelectric effect, *Comput. Mater. Sci.* **108**, 309 (2015).
- [56] Q. Li, C. T. Nelson, S.-L. Hsu, A. R. Damodaran, L.-L. Li, A. K. Yadav, M. McCarter, L. W. Martin, R. Ramesh, and S. V. Kalinin, Quantification of flexoelectricity in $\text{PbTiO}_3/\text{SrTiO}_3$ superlattice polar vortices using machine learning and phase-field modeling, *Nat. Commun.* **8**, 1468 (2017)[].
- [57] A. Stukowski, Computational analysis methods in atomistic modeling of crystals, *JOM* **66**, 399 (2014).
- [58] L. S. Shvindlerman and G. Gottstein, Unexplored topics and potentials of grain boundary engineering, *Scr. Mater.* **54**, 1041 (2006).
- [59] S. Van Petegem, F. Dalla Torre, D. Segers, and H. Van Swygenhoven, Free volume in nanostructured Ni, *Scr. Mater.* **48**, 17 (2003).
- [60] W. Gui-Jin and V. Vitek, Relationships between grain boundary structure and energy, *Acta Metall.* **34**, 951 (1986).
- [61] G. S. Rohrer, The role of grain boundary energy in grain boundary complexion transitions, *Curr. Opin. Solid State Mater. Sci.* **20**, 231 (2016).

- [62] T. Shimada, T. Ueda, J. Wang, and T. Kitamura, Hybrid Hartree-Fock density functional study of charged point defects in ferroelectric PbTiO_3 , [Phys. Rev. B **87**, 174111 \(2013\)](#).
- [63] M. W. Cleveland and M. J. Demkowicz, Persistence of negative vacancy and self-interstitial formation energies in atomistic models of amorphous silicon, [Phys. Rev. Mater. **6**, 013611 \(2022\)](#).
- [64] I. Adlakha, M. A. Tschopp, and K. N. Solanki, The role of grain boundary structure and crystal orientation on crack growth asymmetry in aluminum, [Mater. Sci. Eng. **618**, 345 \(2014\)](#).